

Phonon Linewidths in Twisted Bilayer Graphene near Magic Angle

Shinjan Mandal,¹ Indrajit Maity,² H R Krishnamurthy,^{1,3} and Manish Jain^{1,*}

¹*Center for Condensed Matter Theory, Department of Physics, Indian Institute of Science, Bangalore*

²*Departments of Materials and the Thomas Young Centre for Theory and Simulation of Materials, Imperial College London, South Kensington Campus*

³*International Centre for Theoretical Sciences, Tata Institute of Fundamental Research, Bangalore*

(Dated: July 3, 2024)

We present a computational study of the phonon linewidths in twisted bilayer graphene arising from electron-phonon interactions and anharmonic effects. The electronic structure is calculated using distance-dependent transfer integrals based on the atomistic Slater-Koster tight-binding formalism including electron-electron interactions treated at the Hartree level, and the phonons are calculated using classical force fields. These ingredients are used to calculate the phonon linewidths arising from electron-phonon interactions. Furthermore, anharmonic effects on the linewidths are computed using the mode-projected velocity autocorrelation function obtained from classical molecular dynamics. We predict a moiré potential induced splitting of this mode, which arises due to contributions from high symmetry stacking regions. Our findings show that both electron-phonon and anharmonic effects have a significant impact on the linewidth of the Raman active G mode near the magic angle.

The exceptional electronic and vibrational properties of twisted bilayer graphene (TBG) have fueled significant research interest. The formation of large period moiré structures containing several thousand atoms, arising from a small rotational misalignment between the two graphene sheets in these systems leads to unique properties that are distinct from those of aligned bilayer graphene. These include the emergence of flat bands [1–4], superconductivity near the magic angle of $\sim 1.1^\circ$ twist [1, 5–7], ferromagnetism [8, 9], correlated electronic behaviour [6, 10, 11], and a variety of other exotic electronic properties [12–19]. At small angles, a sample of TBG under experimental conditions also undergoes significant lattice relaxation [20–23]. The electronic and phononic properties of TBG are significantly influenced by these lattice deformations [24–28].

A key debate in the scientific discourse on TBG revolves around the relative importance of electron-phonon (el-ph) and electron-electron interactions in determining the material’s electronic properties, [29–33] especially at the magic angle, where exotic properties are observed [34]. While evidences of correlated electron states have been observed, a comprehensive understanding of the effect of electron-phonon coupling in TBG remains a topic of intense interest in the field.

One experimentally accessible approach to investigate the strength of el-ph interactions is to measure the phonon lifetimes in Raman spectroscopy. The phonon linewidth, which is the inverse of the lifetime, quantifies the decay rate of phonons resulting from various scattering processes caused by el-ph and other interactions. El-ph interactions also play a crucial role in determining the thermal conductivity, electrical resistivity, and mechanical properties of materials [35, 36]. Recent experiments in TBG have revealed the localization of the Raman active G mode [37] as well as a significant enhancement of the G

mode linewidth near the magic angle [38]. Consequently, a theoretical computation of the phonon linewidths is of great interest to the community.

While the computation of the phonon linewidth is essential, first-principles calculations in TBG are extremely challenging due to the large number of atoms in the moiré unit cell. In this letter, we present a computational study of the electron-phonon and phonon-phonon contributions to the phonon linewidth in TBG. Our approach combines an atomistic tight-binding model to compute the electronic structure, classical force fields to model the phonon spectra, and classical molecular dynamics (MD) simulations to account for anharmonic effects. We investigate the influence of the moiré superlattice on the behaviour of the G mode by considering various twist angles in TBG. By systematically varying the twist angle, the doping and the temperature, we explore the impact of the moiré superlattice on the linewidth and provide insights into the electron-phonon and phonon-phonon scattering mechanisms near the magic angle.

Assuming Matthiessen’s rule, the phonon linewidth (Γ) is the sum of the contributions from the electron-phonon interactions ($\Gamma_{\text{el-ph}}$), anharmonic effects (Γ_{anhm}) and disorder effects (Γ_{disod}) [35].

$$\Gamma = \Gamma_{\text{el-ph}} + \Gamma_{\text{anhm}} + \Gamma_{\text{disod}} \quad (1)$$

In a pristine crystal, Γ_{disod} is assumed to be negligible.

Within the framework of many-body perturbation theory, the lifetime arising due to el-ph interaction for a specified phonon mode ($\mathbf{q}s$) of the moiré superlattice is given by [36, 39]:

$$\Gamma_{\text{el-ph}}^{\mathbf{q}s} = \frac{4\pi}{\Omega_{\text{BZ}}} \sum_{m,n} \int d\mathbf{k} |g_{\mathbf{k},\mathbf{q}}^{mns}|^2 (f_{\mathbf{k}}^n - f_{\mathbf{k}+\mathbf{q}}^m) \times \delta(\epsilon_{\mathbf{k}+\mathbf{q}}^m - \epsilon_{\mathbf{k}}^n - \omega_{\mathbf{q}s}) \quad (2)$$

where the el-ph coupling matrix element

$$g_{\mathbf{k},\mathbf{q}}^{mns} = \langle \psi_{\mathbf{k}+\mathbf{q}}^m | \nabla_{\mathbf{q}s} H | \psi_{\mathbf{k}}^n \rangle \quad (3)$$

is the amplitude for the scattering of an electron from the n^{th} electronic band at \mathbf{k} to the m^{th} band at $\mathbf{k} + \mathbf{q}$ by interacting with the phonon mode (\mathbf{q}_s). The n^{th} electronic band at \mathbf{k} has an energy $\epsilon_{\mathbf{k}}^n$ and a Fermi occupation of $f_{\mathbf{k}}^n$, while the phonon mode (\mathbf{q}_s) has energy $\omega_{\mathbf{q}_s}$. We describe below the procedure we use for the evaluation of $g_{\mathbf{k},\mathbf{q}}^{mns}$.

We generate the TBG structures using the TWISTER package [40]. Structural relaxations of the atoms in TBG are performed using classical interatomic potentials implemented in the LAMMPS package [41]. Specifically, we use the Tersoff [42] potential for the intralayer interactions and the DRIP [43] potential for the interlayer interactions. The interlayer separation for the relaxed structure at 1.05° twist is shown in Fig. (1a). To obtain the electronic structure of the relaxed structure we have used an atomistic tight-binding model with distance-dependent Slater-Koster transfer integrals [44].

$$\hat{\mathbf{H}} = - \sum_{i,j} t(\mathbf{r}_i - \mathbf{r}_j) c_i^\dagger c_j + \text{h.c.} \quad (4)$$

The doping-dependent changes to the electronic structure are incorporated into our tight-binding model via on-site Hartree interactions, following ref [45]:

$$V_H(\mathbf{r}) = V(\theta)(\nu - \nu_0) \sum_{j=1,2,3} \cos(\mathbf{G}_j \cdot \mathbf{r}) \quad (5)$$

Here $\nu_0(\theta)$ is the reference doping level where the Hartree potential is zero, $V(\theta)$ is a twist angle dependent energy parameter and \mathbf{G}_j denote the three reciprocal lattice vectors of the moiré unit cell. The parameters for our calculations were obtained from [45]. We compute the force constants required to construct the dynamical matrix, $D(\mathbf{q})$, for the relaxed structures from the same classical interatomic potentials. Diagonalizing $D(\mathbf{q})$ at each \mathbf{q} point we obtain

$$D(\mathbf{q})\Psi_{\mathbf{q}s}^M = \omega_{\mathbf{q}s}^2 \Psi_{\mathbf{q}s}^M \quad (6)$$

$\Psi_{\mathbf{q}s}^M$ is the eigenvector of the moiré phonon mode (\mathbf{q}_s). In the localized atomic orbital framework, the el-ph coupling matrix elements takes the form [46, 47],

$$g_{\mathbf{k},\mathbf{q}}^{mns} = l_{\mathbf{q}s} \sum_{\kappa\alpha} \Psi_{\mathbf{q}s,\kappa\alpha}^M \sum_{pi} \frac{\partial}{\partial x_\alpha} t(\tau_0^\kappa - \tau_p^i) \left(e^{i\mathbf{k}\mathbf{R}_p} \phi_{\mathbf{k}+\mathbf{q},m\kappa}^* \phi_{\mathbf{k},ni} + e^{-i(\mathbf{k}+\mathbf{q})\mathbf{R}_p} \phi_{\mathbf{k}+\mathbf{q},mi}^* \phi_{\mathbf{k},n\kappa} \right) \quad (7)$$

Here τ_p^i denotes the position of the i^{th} atom in the moiré unit cell centered at \mathbf{R}_p , $\phi_{\mathbf{k},ni}$ is the component of the electronic eigenvector for the n^{th} band with the wave vector \mathbf{k} , in the local orbital basis, and $l_{\mathbf{q}s} = \sqrt{\hbar/2M_c\omega_{\mathbf{q}s}}$ is the characteristic length scale associated with each

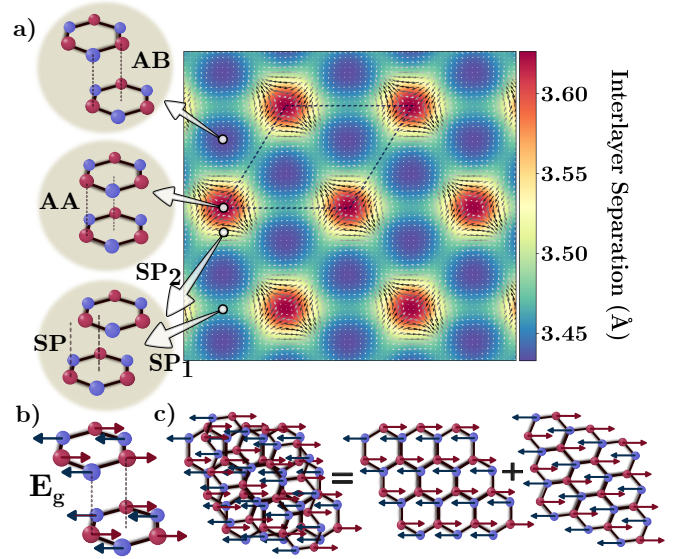


FIG. 1. a) Interlayer separation of 1.05° TBG including atomic relaxations. Atomic structures associated with the different stacking regions (AA, AB, and SP) regions are shown. The gradient of the interlayer separation is shown by the arrows. We can further categorize the SP regions into SP₁ and SP₂ zones by distinguishing between the SP regions which have a higher gradient. b) A schematic of the eigenvectors of the E_g mode at the Γ point in AB stacked bilayer graphene. The direction of displacement of each atom is shown by the corresponding arrows. c) A schematic of the bilayer like E_g mode at the Γ point in twisted bilayer graphene. We assume the displacement of all the A (red dots) and B sites (blue dots) in the supercell to be identical to the corresponding displacements of the A and B atoms in the AB stacked bilayer graphene.

phonon mode, with M_c denoting the mass of a carbon atom. Using eqn.(7) and eqn.(2), we get the contribution from each phonon moiré mode to $\Gamma_{\text{el-ph}}$. In principle, the electron-phonon coupling matrix element would have a further contribution from the gradient of the on-site Hartree term as well. But within our framework, the effect of this term on the computed linewidths turn out to be negligible in the case of TBG. Further details are provided in the Supplementary Information. Previous studies on twisted bilayer transition metal dichalcogenides at finite temperature found that the bandwidth changes were approximately $\sim 2-3$ meV for both the valence and conduction bands [48]. Anticipating a comparable temperature dependence in electronic bandwidths for TBG, we expect that thermal effects on the electronic band structure would not substantially alter the electron-phonon contribution to the linewidth of the G modes (~ 200 meV), and hence have not been considered in these calculations.

In order to calculate the experimentally observed Raman spectra, the Raman intensities for each of the moiré modes should be calculated [49–53]. However, as this

would be prohibitively expensive for angles close to the magic angle, we have chosen a different procedure. Due to the reduced symmetry of the moiré unit cell, the moiré phonon modes cannot be labeled with the irreducible representations of the D_{3d} group. To take the effects of the relaxation into account, at $\mathbf{q} = \mathbf{0}$, we can define a bilayer-like mode in the relaxed moiré unit cell by translating the in-plane G mode atomic displacements in AB stacked bilayer graphene (Fig (1b)) to the corresponding atoms in the moiré (Fig (1c)). We denote the eigenvector for this bilayer-like G mode in the moire unit cell as $\psi_{\mathbf{0}E_g}^{\text{bl}}$. The linewidth arising from each moiré phonon mode is computed by projecting the moiré unit cell phonon modes onto this bilayer-like phonon mode and constructing a spectral function as

$$A_{\mathbf{0}E_g}(\omega) = \frac{1}{\pi} \sum_s \frac{|\langle \Psi_{\mathbf{0}s}^M | \psi_{\mathbf{0}E_g}^{\text{bl}} \rangle|^2 \Gamma_{\text{el-ph}}^{\mathbf{0}s}}{(\omega - \omega_{\mathbf{0}s})^2 + (\Gamma_{\text{el-ph}}^{\mathbf{0}s})^2} \quad (8)$$

Fitting a Lorentzian to this spectral function, we obtain the el-ph linewidth corresponding to the bilayer-like unit cell phonon mode. The results are shown in Figs. 2a and 2b. Previous investigations into the computation of G mode linewidths in TBG near the magic angle [38] employed a method similar to ours, where linewidths were calculated for both Raman active and inactive (or weakly active) modes via Eqn. (7) and the eventual linewidth of the G mode was obtained by employing weight factors that effectively filtered out the contributions from the Raman-inactive modes. In our approach of constructing the spectral function, we capture the G-mode-like characteristics of moiré modes, incorporating their frequencies as well. This comprehensive approach provides an improved understanding of the anticipated Raman activity across the frequency spectrum.

Fig 2c shows that there is a systematic splitting of the projected weights of the moiré mode onto the bilayer-like G mode with decreasing twist angle, resulting in two distributions: a high-frequency distribution (around 1700 cm^{-1}), which we call the E_g^+ distribution, and a low-frequency distribution (around 1680 cm^{-1}), which we call the E_g^- distribution. This splitting can be understood in the context of a nearly free phonon model, which has shown that gaps in the phonon bands of periodic structures can arise due to the effect of an underlying secondary long-period potential. The strength of this potential modulates the size of the gap [54]. In the case of twisted bilayer graphene, the moiré superlattice creates a secondary long-period moiré potential that splits the phonon bands [55]. The increase in the split of the G mode as a function of twist near the magic angle shows that the moiré potential becomes stronger as one approaches the magic angle.

We show the linewidths of E_g^+ and E_g^- mode of the moiré unit cell obtained as a function of doping for several twist angles around the magic angle Fig(2a). The

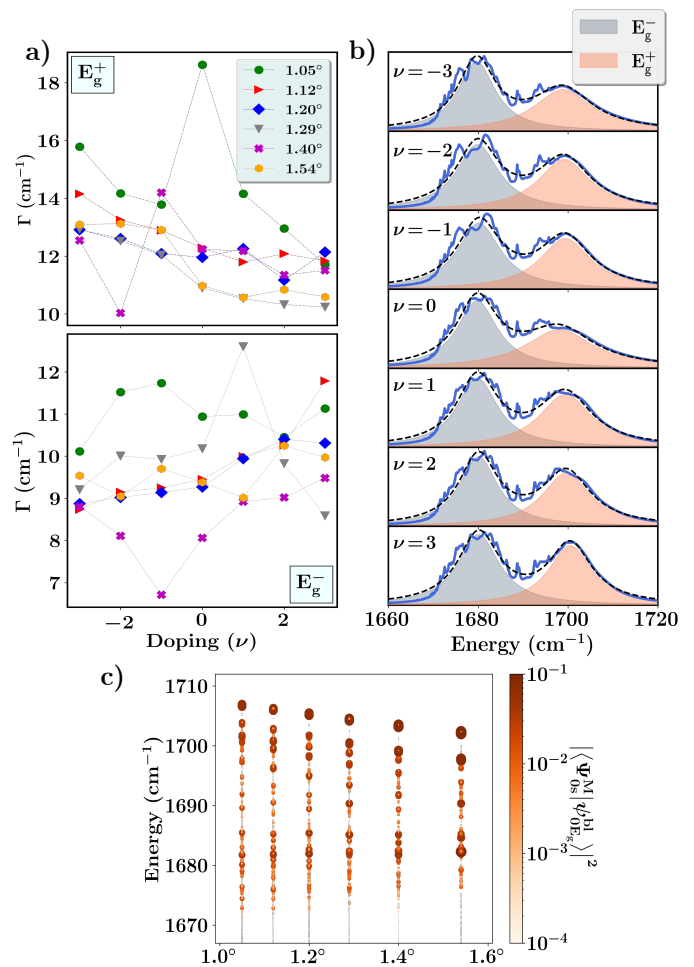


FIG. 2. a) The el-ph interaction induced linewidths of the E_g^+ (top) and the E_g^- (bottom) modes as a function of doping for twist angles near the magic angle. b) A representative fit for the el-ph spectral function at different dopings (ν) is shown for the twist angle of 1.05°. The fits for the other angles are available in the Supplementary Information. c) The projection of the moiré modes ($\Psi_{\mathbf{0}s}^M$) onto the bilayer-like E_g modes $\psi_{\mathbf{0}E_g}^{\text{bl}}$ as a function of twist angle. The colours, as well as the sizes of the points, indicate the weights of the corresponding moiré modes.

linewidth of the E_g^+ mode decreases as doping increases (from -3 to +3), while the linewidth of the E_g^- mode increases as doping increases. The anomalous increase in the linewidth of the E_g^+ mode at $\nu = 0$ for 1.05° can be explained by the joint electronic density of states (JDOS). The peak in the JDOS aligns with the energy distribution of the E_g^+ mode, which results in an increase in the number of scattering channels due to the phonon, and hence an enhanced linewidth (see Fig S9 in the Supplementary Information).

In the low-angle regime, atomic relaxation leads to the formation of high-symmetry stacking regions with differential strain profiles. Previous studies have shown that this variation in the strain profile localizes the G modes

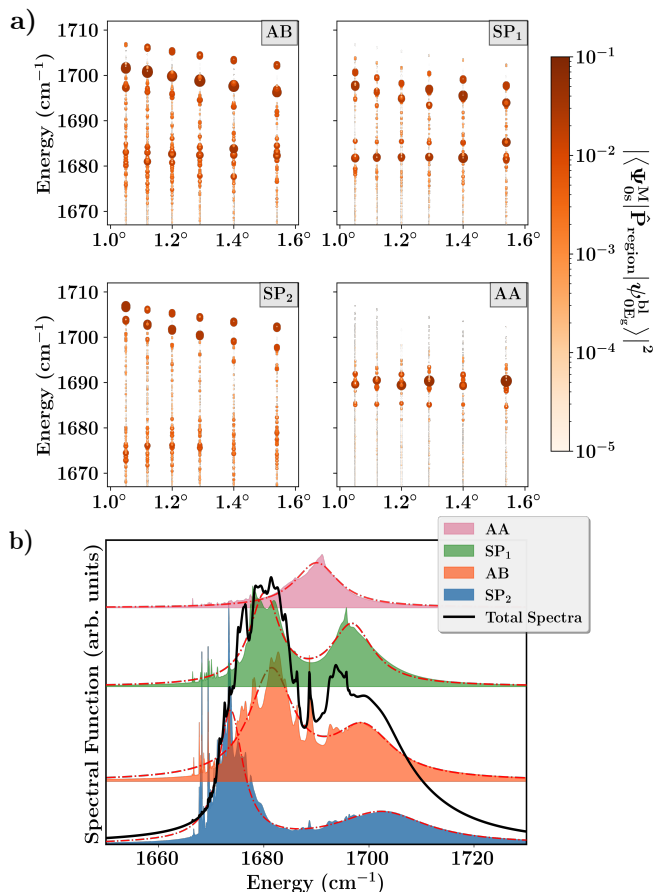


FIG. 3. a) The projections of Ψ_{0s}^M onto the bilayer like E_g mode in different solitonic regions of the moiré cell. b) The projected spectral functions for 1.05° TBG at $\nu = 0$ (4th panel in Fig 2b) projected onto different regions of the moiré. The red dashed lines show the best fit to the data.

[37]. We have identified the stacking regions by examining the interlayer separation between the two graphene layers. As shown in Fig (1a) the AA and the AB stacked regions are easily identified by their respective interlayer distances. In previous studies, the transition region between the AA and the AB was denoted as the saddle point (SP) region [37]. In our analysis we further distinguish two types of saddle point regions, SP_1 and SP_2 . In terms of the in-plane gradient of the interlayer separation, we can see that SP_1 , the transition region between two adjacent AB solitonic regions, has a smaller magnitude of the gradient than SP_2 , the transition region between an AA and an AB solitonic regions. We can project the moiré modes onto the components of $\psi_{0E_g}^{bl}$ arising from the four stacking regions, $|\langle \Psi_{0s}^M | \hat{P}_{\text{region}} | \psi_{0E_g}^{bl} \rangle|^2$. As shown in Fig. 3a, we find that both high frequency and low frequency modes have some localization characteristics. In the AB region, the high-frequency moiré modes have significant weights, while the low-frequency modes have smaller but non-negligible weights. The SP_1 region

has signatures of both high and low frequency modes, while the SP_2 region has significantly higher weights for the high-frequency modes. The projection on the AA region shows that the modes at $\sim 1690 \text{ cm}^{-1}$ are almost entirely localized there consistently for all twist angles considered in this study. This frequency is close to the E_g mode frequency of untwisted bilayer graphene (1690.96 cm^{-1}), which is obtained using the same force fields employed in our calculations.

The identification of the localized phonon modes provides a new perspective for analyzing the spectral functions computed using eqn. (8). We observe seven distinct frequency regions across the four stacking regions, where the projections onto the unit cell modes have significant weight. For each stacking region we plot the spectral function

$$A_{0E_g}^{\text{region}}(\omega) = \frac{1}{\pi} \sum_s \frac{|\langle \Psi_{0s}^M | \hat{P}_{\text{region}} | \psi_{0E_g}^{bl} \rangle|^2 \Gamma_{\text{el-ph}}^{0s}}{(\omega - \omega_{0s})^2 + (\Gamma_{\text{el-ph}}^{0s})^2} \quad (9)$$

The region projected spectral function for 1.05° TBG at $\nu = 0$ is shown in Fig 3b. Additional plots for different angles near the magic angle at integer fillings demonstrating similar behaviour are shown in the Supplementary Information. Fitting the spectral function of the G mode in TBG near the magic angle with Lorentzian functions centered around the seven distinct frequencies, each of which corresponds to a unique contribution from a specific solitonic region, enables a more nuanced interpretation of the underlying physical mechanisms that govern the spectral function.

The anharmonic contribution to the linewidth, Γ_{anhm} , is calculated from the mode projected velocity autocorrelation function (MVACF) [28] of the bilayer like E_g mode. The power spectrum constructed by taking the Fourier transform of the MVACF contains information about the line shift and linewidth of the projected phonon mode at different temperatures. Details about computation of the MVACF are provided in the Supplementary Information.

Similar to the el-ph interaction contributions to the E_g mode spectrum, the MVACF power spectrum is also expected to separate into E_g^+ and E_g^- regions. However, unlike the el-ph interaction induced spectra, performing a spatial analysis on the MVACF spectra is non-trivial. The dynamics of the stacking regions under MD simulations make them difficult to identify. Time averaged stacking regions could potentially be defined by examining the dynamics of the solitonic regions for a finite time, but such an analysis has not been attempted in this work.

The classical force fields used in our computations do not account for doping effects because they lack parametric dependence on the electronic interactions. Therefore, the anharmonic linewidths of the E_g^+ and E_g^- modes are independent of doping. Consequently, the total linewidth (Γ) obtained at each doping for a particular angle is

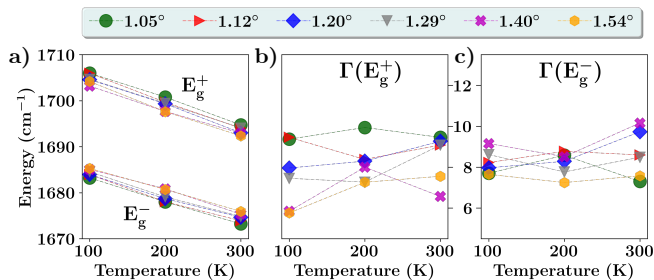


FIG. 4. (a) The lineshifts arising from the anharmonic interactions for the E_g^+ and E_g^- modes as a function of Temperature. The corresponding linewidths (Γ_{anhm}) obtained at different temperatures for each angle are also shown for E_g^+ (b) and E_g^- (c) modes. The units for the reported linewidths are cm^{-1} .

equivalent to the el-ph linewidth $\Gamma_{\text{el-ph}}$ at the particular doping shifted by a constant amount (eqn.1) Fitting Lorentzians to the MVACF power spectrum yields the lineshifts and linewidths of the E_g^+ and E_g^- modes. The lineshifts of the modes are shown in the left panel of Fig 4. For both E_g^+ and E_g^- , the modes soften by approximately 10 cm^{-1} on increasing the temperature from 100K to 300K. The linewidths of these two modes for different twist angles are shown as a function of temperature in the center and right panels of Fig (4) respectively.

In summary, in this theoretical investigation we have computed the contributions of el-ph and ph-ph interactions to the linewidth of the G mode phonon in TBG. The modulation of the moiré potential due to the twist angle introduces gaps in the phonon mode spectra at the Γ point near the magic angle. We expect that this split of $\sim 20 \text{ cm}^{-1}$ in the E_g mode will be observable in Raman measurements. Our el-ph calculations show a systematic increase/decrease in the el-ph linewidth of the E_g^+ and E_g^- modes as a function of electron doping. The ph-ph scattering calculations show a similar split of the G mode into E_g^+ and E_g^- . The linewidths arising from ph-ph scattering do not change significantly as a function of temperature.

The authors thank Kemal Atalar and Valerio Vitale for useful discussions over the course of the project and Darshit Solanki for inputs during the analysis of the data. M.J. acknowledges the National Supercomputing Mission of the Department of Science and Technology, India, and Nano Mission of the Department of Science and Technology for financial support under Grants No. DST/NSM/R&D.HPC_Applications/2021/23 and No. DST/NM/TUE/QM-10/2019 respectively. H.R.K. acknowledges the Science and Engineering Research Board of the Department of Science and Technology, India, and the Indian National Science Academy for support under Grants No. SB/DF/005/2017 and No. INSA/SP/SS/2023/ respectively. H.R.K. also acknowledges support in ICTS by a grant from the Simons Foun-

ation (677895, R.G.). I.M. acknowledges funding from the European Union's Horizon 2020 research and innovation program under the Marie Skłodowska-Curie Grant agreement No. 101028468.

* mjain@iisc.ac.in

- [1] Y. Cao, V. Fatemi, S. Fang, K. Watanabe, T. Taniguchi, E. Kaxiras, and P. Jarillo-Herrero, *Nature* **556**, 43 (2018).
- [2] S. Lisi, X. Lu, T. Benschop, T. A. de Jong, P. Stepanov, J. R. Duran, F. Margot, I. Cucchi, E. Cappelli, A. Hunter, *et al.*, *Nature Physics* **17**, 189 (2021).
- [3] M. I. B. Utama, R. J. Koch, K. Lee, N. Leconte, H. Li, S. Zhao, L. Jiang, J. Zhu, K. Watanabe, T. Taniguchi, *et al.*, *Nature Physics* **17**, 184 (2021).
- [4] F. Mesple, A. Missaoui, T. Cea, L. Huder, F. Guinea, G. T. de Laissardiere, C. Chapelier, and V. T. Renard, *Physical Review Letters* **127**, 126405 (2021).
- [5] M. Yankowitz, S. Chen, H. Polshyn, Y. Zhang, K. Watanabe, T. Taniguchi, D. Graf, A. F. Young, and C. R. Dean, *Science* **363**, 1059 (2019).
- [6] X. Lu, P. Stepanov, W. Yang, M. Xie, M. A. Aamir, I. Das, C. Urgell, K. Watanabe, T. Taniguchi, G. Zhang, *et al.*, *Nature* **574**, 653 (2019).
- [7] M. Oh, K. P. Nuckolls, D. Wong, R. L. Lee, X. Liu, K. Watanabe, T. Taniguchi, and A. Yazdani, *Nature* **600**, 240 (2021).
- [8] A. L. Sharpe, E. J. Fox, A. W. Barnard, J. Finney, K. Watanabe, T. Taniguchi, M. Kastner, and D. Goldhaber-Gordon, *Science* **365**, 605 (2019).
- [9] C. Tschirhart, M. Serlin, H. Polshyn, A. Shragai, Z. Xia, J. Zhu, Y. Zhang, K. Watanabe, T. Taniguchi, M. Huber, *et al.*, *Science* **372**, 1323 (2021).
- [10] Y. Cao, V. Fatemi, A. Demir, S. Fang, S. L. Tomarken, J. Y. Luo, J. D. Sanchez-Yamagishi, K. Watanabe, T. Taniguchi, E. Kaxiras, *et al.*, *Nature* **556**, 80 (2018).
- [11] Y. Saito, J. Ge, K. Watanabe, T. Taniguchi, and A. F. Young, *Nature Physics* **16**, 926 (2020).
- [12] A. Kerelsky, L. J. McGilly, D. M. Kennes, L. Xian, M. Yankowitz, S. Chen, K. Watanabe, T. Taniguchi, J. Hone, C. Dean, *et al.*, *Nature* **572**, 95 (2019).
- [13] S. Shallcross, S. Sharma, and O. A. Pankratov, *Physical Review Letters* **101**, 056803 (2008).
- [14] S. Shallcross, S. Sharma, E. Kandelaki, and O. Pankratov, *Physical Review B* **81**, 165105 (2010).
- [15] N. N. Nam and M. Koshino, *Physical Review B* **96**, 075311 (2017).
- [16] B. Ghawri, P. S. Mahapatra, M. Garg, S. Mandal, S. Bhowmik, A. Jayaraman, R. Soni, K. Watanabe, T. Taniguchi, H. R. Krishnamurthy, *et al.*, *Nature Communications* **13**, 1522 (2022).
- [17] K. P. Nuckolls, M. Oh, D. Wong, B. Lian, K. Watanabe, T. Taniguchi, B. A. Bernevig, and A. Yazdani, *Nature* **588**, 610 (2020).
- [18] H. Polshyn, M. Yankowitz, S. Chen, Y. Zhang, K. Watanabe, T. Taniguchi, C. R. Dean, and A. F. Young, *Nature Physics* **15**, 1011 (2019).
- [19] Y. Cao, D. Chowdhury, D. Rodan-Legrain, O. Rubies-Bigorda, K. Watanabe, T. Taniguchi, T. Senthil, and P. Jarillo-Herrero, *Physical Review Letters* **124**, 076801

- (2020).
- [20] A. M. Popov, I. V. Lebedeva, A. A. Knizhnik, Y. E. Lozovik, and B. V. Potapkin, *Physical Review B* **84**, 045404 (2011).
- [21] J. S. Alden, A. W. Tsen, P. Y. Huang, R. Hovden, L. Brown, J. Park, D. A. Muller, and P. L. McEuen, *Proceedings of the National Academy of Sciences* **110**, 11256 (2013).
- [22] H. Yoo, R. Engelke, S. Carr, S. Fang, K. Zhang, P. Cazeaux, S. H. Sung, R. Hovden, A. W. Tsen, T. Taniguchi, *et al.*, *Nature materials* **18**, 448 (2019).
- [23] S. Carr, D. Massatt, S. B. Torrisi, P. Cazeaux, M. Luskin, and E. Kaxiras, *Physical Review B* **98**, 224102 (2018).
- [24] K. Uchida, S. Furuya, J.-I. Iwata, and A. Oshiyama, *Physical Review B* **90**, 155451 (2014).
- [25] S. Huang, K. Kim, D. K. Efimkin, T. Lovorn, T. Taniguchi, K. Watanabe, A. H. MacDonald, E. Tutuc, and B. J. LeRoy, *Physical Review Letters* **121**, 037702 (2018).
- [26] P. Lucignano, D. Alfè, V. Cataudella, D. Ninno, and G. Cantele, *Physical Review B* **99**, 195419 (2019).
- [27] M. Koshino and Y.-W. Son, *Physical Review B* **100**, 075416 (2019).
- [28] I. Maity, M. H. Naik, P. K. Maiti, H. R. Krishnamurthy, and M. Jain, *Physical Review Research* **2**, 013335 (2020).
- [29] F. Wu, A. H. MacDonald, and I. Martin, *Physical Review Letters* **121**, 257001 (2018).
- [30] M. Koshino, N. F. Yuan, T. Koretsune, M. Ochi, K. Kuroki, and L. Fu, *Physical Review X* **8**, 031087 (2018).
- [31] C.-C. Liu, L.-D. Zhang, W.-Q. Chen, and F. Yang, *Physical Review Letters* **121**, 217001 (2018).
- [32] F. Wu, E. Hwang, and S. D. Sarma, *Physical Review B* **99**, 165112 (2019).
- [33] B. A. Bernevig and D. K. Efetov, *Physics Today* **77**, 38 (2024).
- [34] S. D. Sarma and F. Wu, *Annals of Physics* **417**, 168193 (2020).
- [35] G. Grimvall, *Physica Scripta* **14**, 63 (1976).
- [36] F. Giustino, *Rev. Mod. Phys.* **89**, 015003 (2017).
- [37] A. C. Gadelha, D. A. Ohlberg, C. Rabelo, E. G. Neto, T. L. Vasconcelos, J. L. Campos, J. S. Lemos, V. Ornelas, D. Miranda, R. Nadas, *et al.*, *Nature* **590**, 405 (2021).
- [38] A. C. Gadelha, V.-H. Nguyen, E. G. Neto, F. Santana, M. B. Raschke, M. Lamparski, V. Meunier, J.-C. Charlier, and A. Jorio, *Nano letters* **22**, 6069 (2022).
- [39] C.-H. Park, F. Giustino, M. L. Cohen, and S. G. Louie, *Nano letters* **8**, 4229 (2008).
- [40] S. Naik, M. H. Naik, I. Maity, and M. Jain, *Computer Physics Communications* **271**, 108184 (2022).
- [41] A. P. Thompson, H. M. Aktulga, R. Berger, D. S. Bolintineanu, W. M. Brown, P. S. Crozier, P. J. in't Veld, A. Kohlmeyer, S. G. Moore, T. D. Nguyen, *et al.*, *Computer Physics Communications* **271**, 108171 (2022).
- [42] A. Kinaci, J. B. Haskins, C. Sevik, and T. Çağın, *Physical Review B* **86**, 115410 (2012).
- [43] M. Wen, S. Carr, S. Fang, E. Kaxiras, and E. B. Tadmor, *Physical Review B* **98**, 235404 (2018).
- [44] J. C. Slater and G. F. Koster, *Physical Review* **94**, 1498 (1954).
- [45] Z. A. Goodwin, V. Vitale, X. Liang, A. A. Mostofi, and J. Lischner, *Electronic Structure* **2**, 034001 (2020).
- [46] L. A. Agapito and M. Bernardi, *Physical Review B* **97**, 235146 (2018).
- [47] Y. W. Choi and H. J. Choi, *Physical Review B* **98**, 241412 (2018).
- [48] I. Maity, A. A. Mostofi, and J. Lischner, *Nano Letters* **23**, 4870 (2023).
- [49] A. I. Cocemasov, D. L. Nika, and A. A. Balandin, *Phys. Rev. B* **88**, 035428 (2013).
- [50] E. Cappelluti, J. A. Silva-Guillén, H. Rostami, and F. Guinea, *Phys. Rev. B* **108**, 125401 (2023).
- [51] K. Sato, R. Saito, C. Cong, T. Yu, and M. S. Dresselhaus, *Physical Review B* **86**, 125414 (2012).
- [52] R. Saito, T. Takeya, T. Kimura, G. Dresselhaus, and M. Dresselhaus, *Physical Review B* **57**, 4145 (1998).
- [53] A. Jorio, M. S. Dresselhaus, R. Saito, and G. Dresselhaus, *Raman spectroscopy in graphene related systems* (John Wiley & Sons, 2011).
- [54] B. Van Troeye, M. Lamparski, N. Sheremetyeva, and V. Meunier, *Physical Review B* **105**, 035420 (2022).
- [55] T. Ohta, J. T. Robinson, P. J. Feibelman, A. Bostwick, E. Rotenberg, and T. E. Beechem, *Phys. Rev. Lett.* **109**, 186807 (2012).

Supplementary: Phonon Linewidths in Twisted Bilayer Graphene near Magic Angle

Shinjan Mandal,¹ Indrajit Maity,² H R Krishnamurthy,^{1,3} and Manish Jain^{1,*}

¹Center for Condensed Matter Theory, Department of Physics, Indian Institute of Science, Bangalore

²Departments of Materials, Imperial College London, South Kensington Campus

³International Centre for Theoretical Sciences, Tata Institute of Fundamental Research, Bangalore

(Dated: July 3, 2024)

STRUCTURE GENERATION AND RELAXATION

We generate the rigid TBG structures using the TWISTER code [1] and perform the atomic relaxation in LAMMPS [2] using Tersoff [3] as the intralayer potential and DRIP [4] as the interlayer potential. The systems are relaxed upto a force tolerance of 10^{-6} eV/Å.

The choice of Tersoff over other standard potentials like LCBOP or AIREBO was intentional even though the phonon frequencies of the high energy optical modes computed with this potential are grossly overestimated. The temperature dependence of the G modes computed with Tersoff shows the correct qualitative behaviour, unlike other potentials where significant hardening of the modes is observed with rising temperature, contrary to experimental observations [5]. Since we have computed the contributions due to the anharmonic effects as well, ensuring the correct temperature dependence of the G-mode was crucial for our calculations.

ELECTRONIC STRUCTURE

The electronic hamiltonian of the system is

$$\hat{H} = - \sum_{i,j} t(\mathbf{r}_i - \mathbf{r}_j) c_i^\dagger c_j + \text{h.c.} = - \sum_{i,j} t_{ij} c_i^\dagger c_j + \text{h.c.} \quad (1)$$

where \mathbf{r}_i denotes the real space position of the i^{th} atom, and c_i^\dagger and c_i are the creation and annihilation operators at \mathbf{r}_i . We approximate the transfer integrals t_{ij} using the Slater-Koster formalism [6] assuming that the overlap of the p_z orbitals can be approximated as the linear combination of the $\sigma\sigma$ and $\pi\pi$ overlaps. Taking the local curvature of the sheets into account the transfer integral can be written as [7]:

$$t_{ij} = t_{\pi\pi} [\hat{\mathbf{n}}_i - (\hat{\mathbf{n}}_i \cdot \hat{\mathbf{r}}_{ij}) \hat{\mathbf{r}}_{ij}] \cdot [\hat{\mathbf{n}}_j - (\hat{\mathbf{n}}_j \cdot \hat{\mathbf{r}}_{ij}) \hat{\mathbf{r}}_{ij}] + t_{\sigma\sigma} [\hat{\mathbf{n}}_i \cdot \hat{\mathbf{r}}_{ij}] \cdot [\hat{\mathbf{n}}_j \cdot \hat{\mathbf{r}}_{ij}] \quad (2)$$

where $\hat{\mathbf{n}}_i$ is the unit normal at the i^{th} site, and $\hat{\mathbf{r}}_{ij}$ is the unit vector joining the sites \mathbf{r}_i and \mathbf{r}_j . The terms $t_{\pi\pi}$ and $t_{\sigma\sigma}$ are taken as follows:

$$\begin{aligned} t_{\pi\pi} &= t_{\pi}^0 \exp\left(-\frac{\mathbf{r}_{ij} - a_0}{\delta}\right); & t_{\pi}^0 &= -2.7 \text{ eV} \\ t_{\sigma\sigma} &= t_{\sigma}^0 \exp\left(-\frac{\mathbf{r}_{ij} - d_0}{\delta}\right); & t_{\sigma}^0 &= 0.48 \text{ eV} \end{aligned} \quad (3)$$

The parameter $a_0 = 1.42$ Å is taken as the nearest neighbour distance, $d_0 = 3.35$ Å and the attenuating factor, $\delta = 0.184\sqrt{3}a_0$ is chosen so that the strength of the second nearest neighbor transfer integral is 0.1 times that of the first neighbour.[8]

The Hartree interaction is modelled as an onsite term:

$$V_H(r) \approx V(\theta)(\nu - \nu_0(\theta)) \sum_{j=1,2,3} \cos(\mathbf{G}_j \cdot \mathbf{r}) \quad (4)$$

Here ν is the filling and \mathbf{G}_j are the three reciprocal lattice vectors used to describe the out-of-plane corrugation of the TBG. The parameters $\nu_0(\theta)$ and $V(\theta)$ have been provided in Ref.[9]. The resulting electronic densities of states (DOS) for the various angles we have studied are shown in Fig. S1.

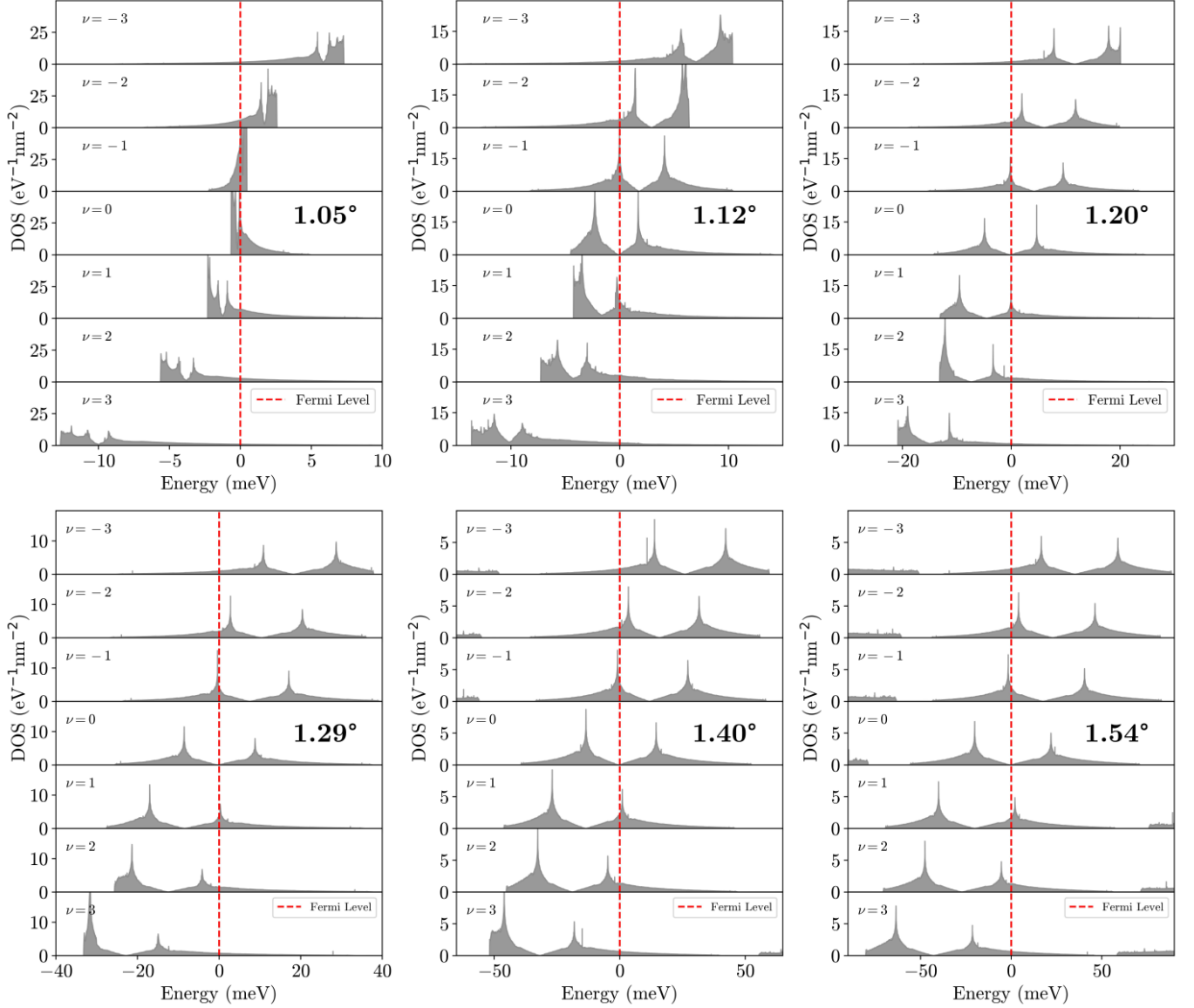


FIG. S1. Density of states for the systems we have studied, as a function of the filling ν . The electronic structures were computed after putting in the effects of the Hartree interactions [9]

PHONON CALCULATIONS

The force constants were generated via a finite difference method from the classical force fields mentioned before.

$$\Phi_{\alpha\beta}^{j0,j'l'} = \frac{\partial^2 V}{\partial \mathbf{r}_{\alpha}^{j0} \partial \mathbf{r}_{\beta}^{j'l'}} \quad (5)$$

where \mathbf{r}_{α}^{jl} denotes component of the position of the j^{th} atom in the l^{th} unit cell in the Cartesian direction α . The dynamical matrix is given by

$$D_{\alpha\beta}^{jj'}(\mathbf{q}) = \frac{1}{\sqrt{m_j m_{j'}}} \sum_{l'} \Phi_{\alpha\beta}^{j0,j'l'} e^{i\mathbf{q} \cdot (\mathbf{r}_{j'l'} - \mathbf{r}_{j0})} \quad (6)$$

To obtain the moiré phonon spectrum at each \mathbf{q} point, we need to solve the eigenvalue equation

$$D(\mathbf{q})\Psi_{\mathbf{q}\nu}^{\mathbf{M}} = \omega_{\mathbf{q}\nu}^2 \Psi_{\mathbf{q}\nu}^{\mathbf{M}} \quad (7)$$

The AB stacked bilayer graphene phonon modes obtained using the potentials are shown in Fig S2.

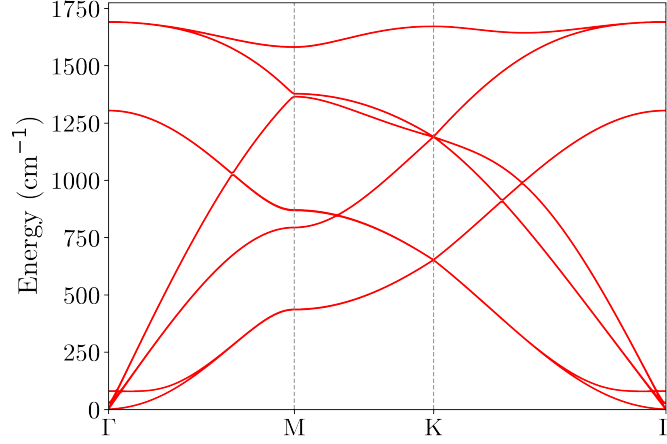


FIG. S2. Phonon modes in AB stacked bilayer graphene

Identification of the modes

The bilayer modes were analyzed by plotting the eigenvectors at the Γ point. The projections in the planes perpendicular to each Cartesian direction are shown in Fig S3,S4 and S5. The blue dots denote the atoms in the top layer while the red dots are the atoms in the bottom layer. The arrows show the displacement of the atoms in the direction of the eigenvector. From these projections, we can identify the E_g modes in the bilayer system. The frequencies corresponding to each mode are also shown.

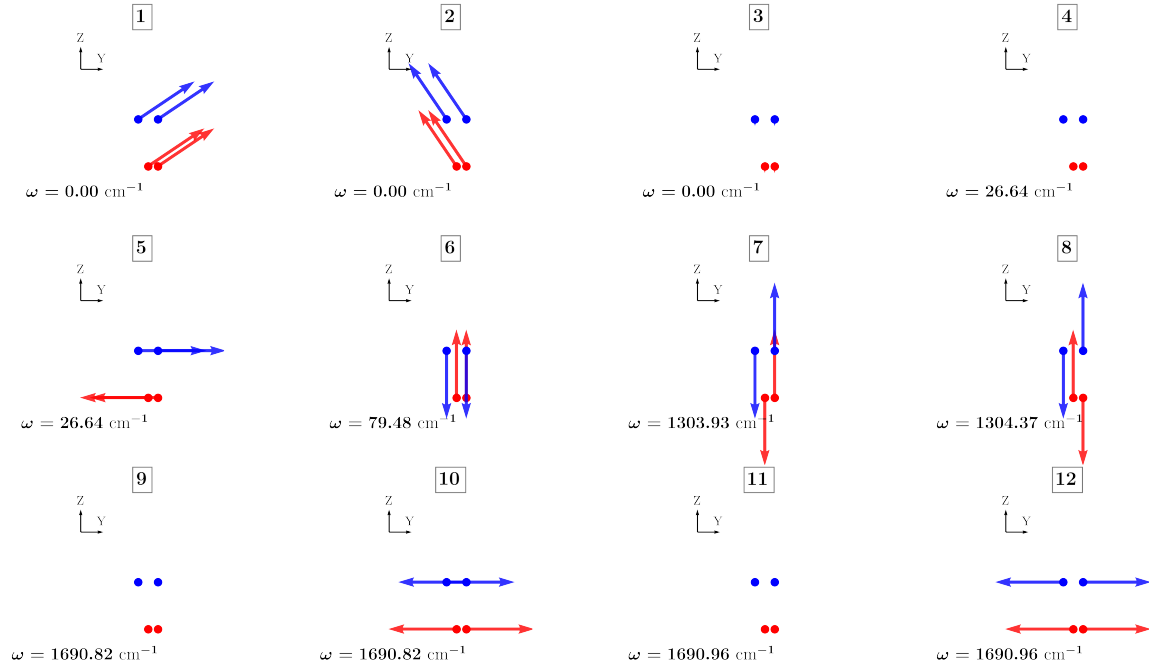


FIG. S3. X-projections of the unit cell Γ phonons in AB stacked bilayer graphene

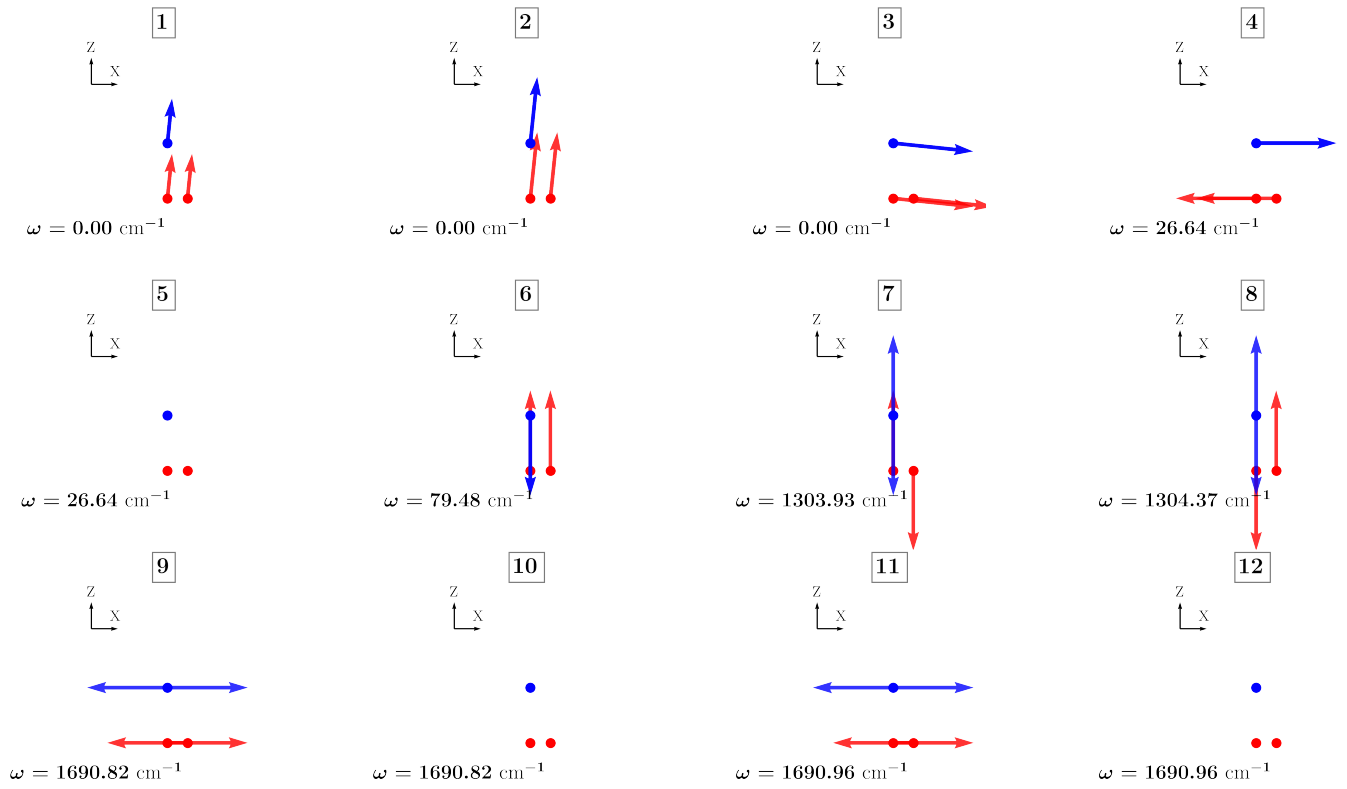


FIG. S4. Y-projections of the unit cell Γ phonons in AB stacked bilayer graphene

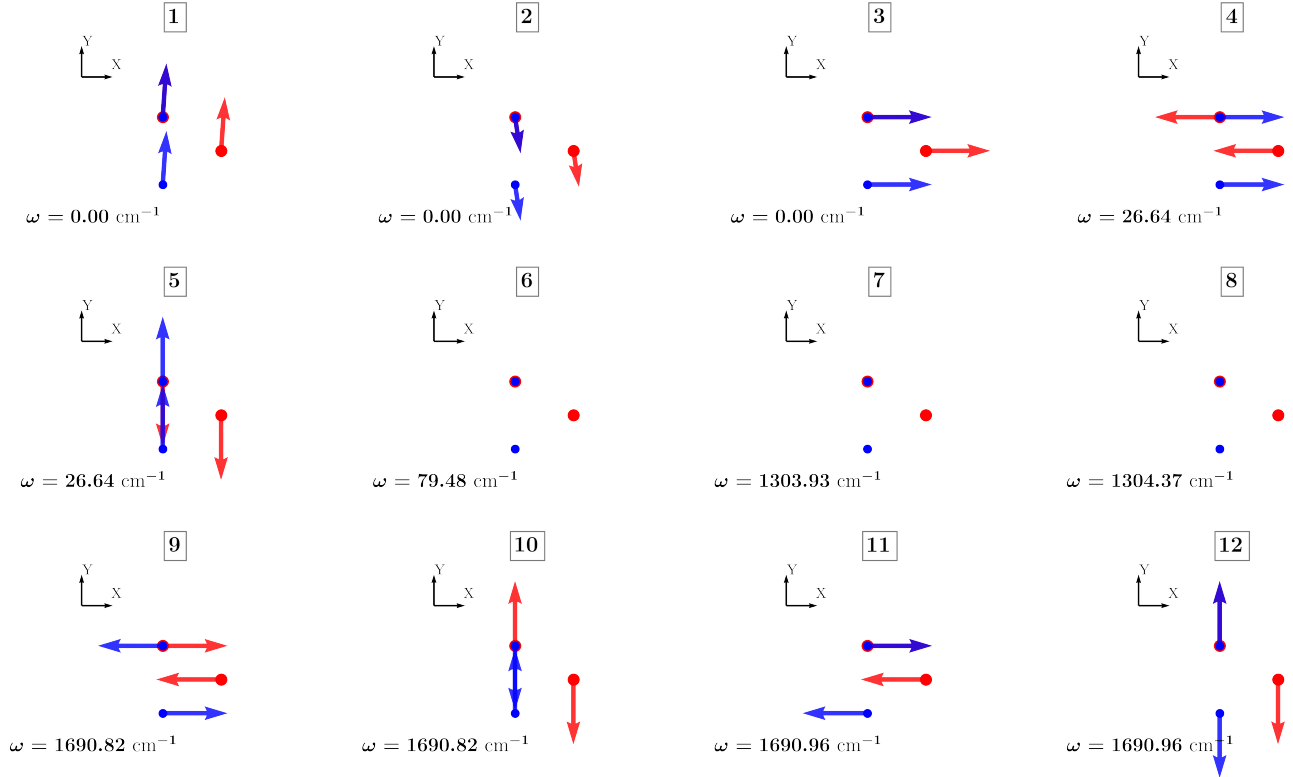


FIG. S5. Z-projections of the unit cell Γ phonons in AB stacked bilayer graphene

ELECTRON-PHONON CALCULATIONS

Benchmarking

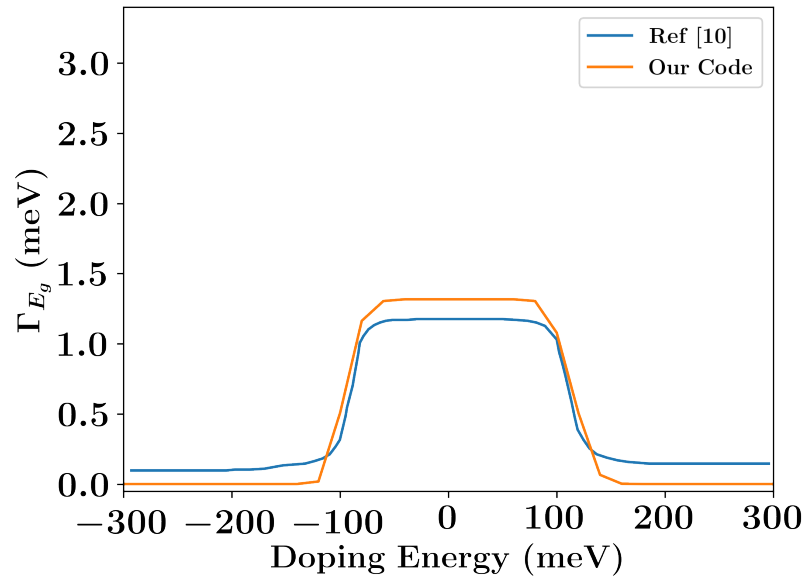


FIG. S6. E_g mode linewidth in AB bilayer from our approach compared with first principles results from [10]

FITS TO THE EL-PH SPECTRAL FUNCTIONS

Although the spectral functions plots from eqn.(8) of the main text may resemble Raman intensity plots, it is crucial to recognize that they are not equivalent. While the positions of the Raman peaks and their associated linewidths are likely correctly extracted by fitting Lorentzians to the spectral function, the spectral function values themselves should not be misconstrued as corresponding to the measured Raman intensities.

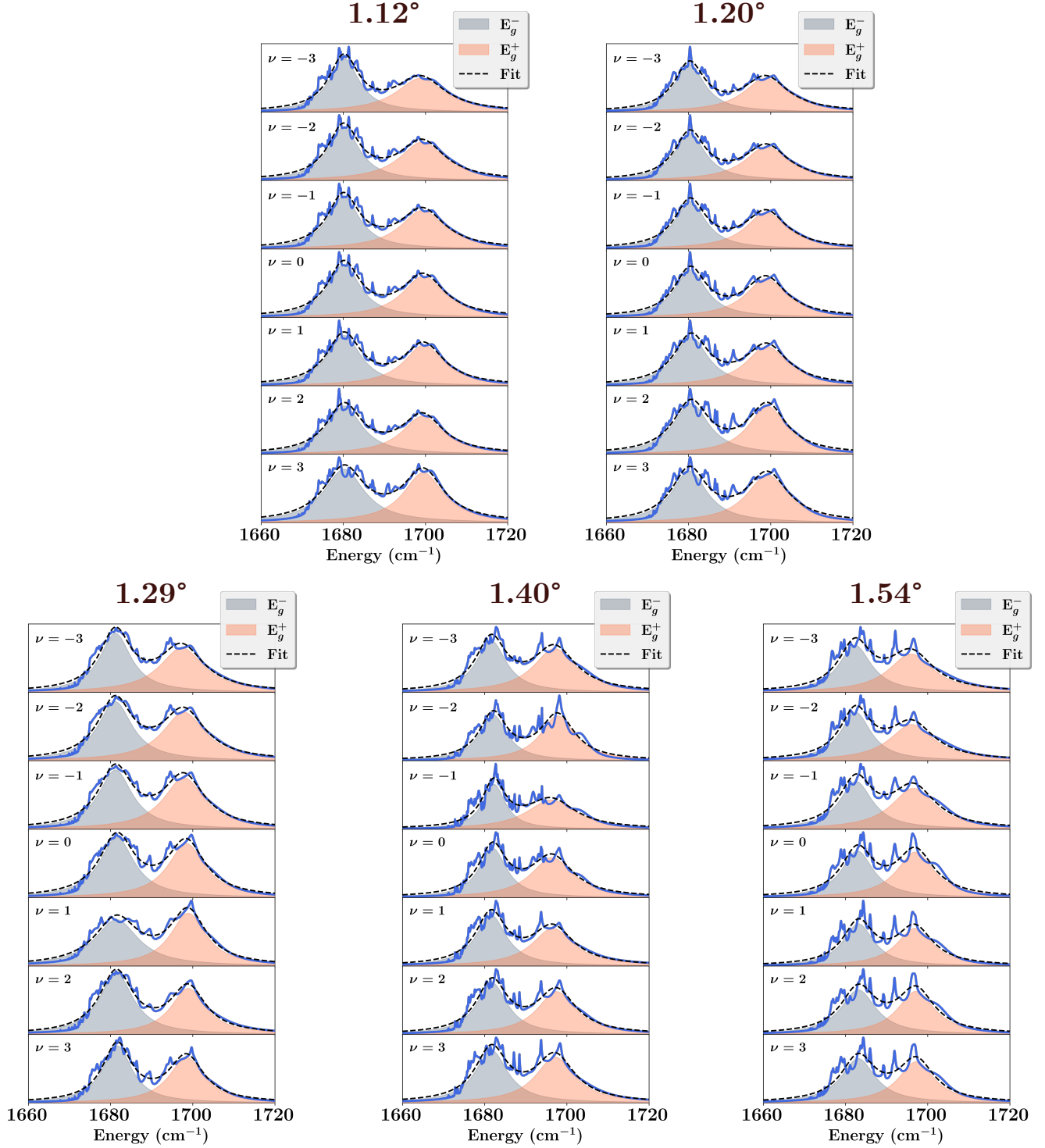


FIG. S7. Lorentzian fits for the electron-phonon spectral function

SPATIAL RESOLUTION OF THE SPECTRAL FUNCTION

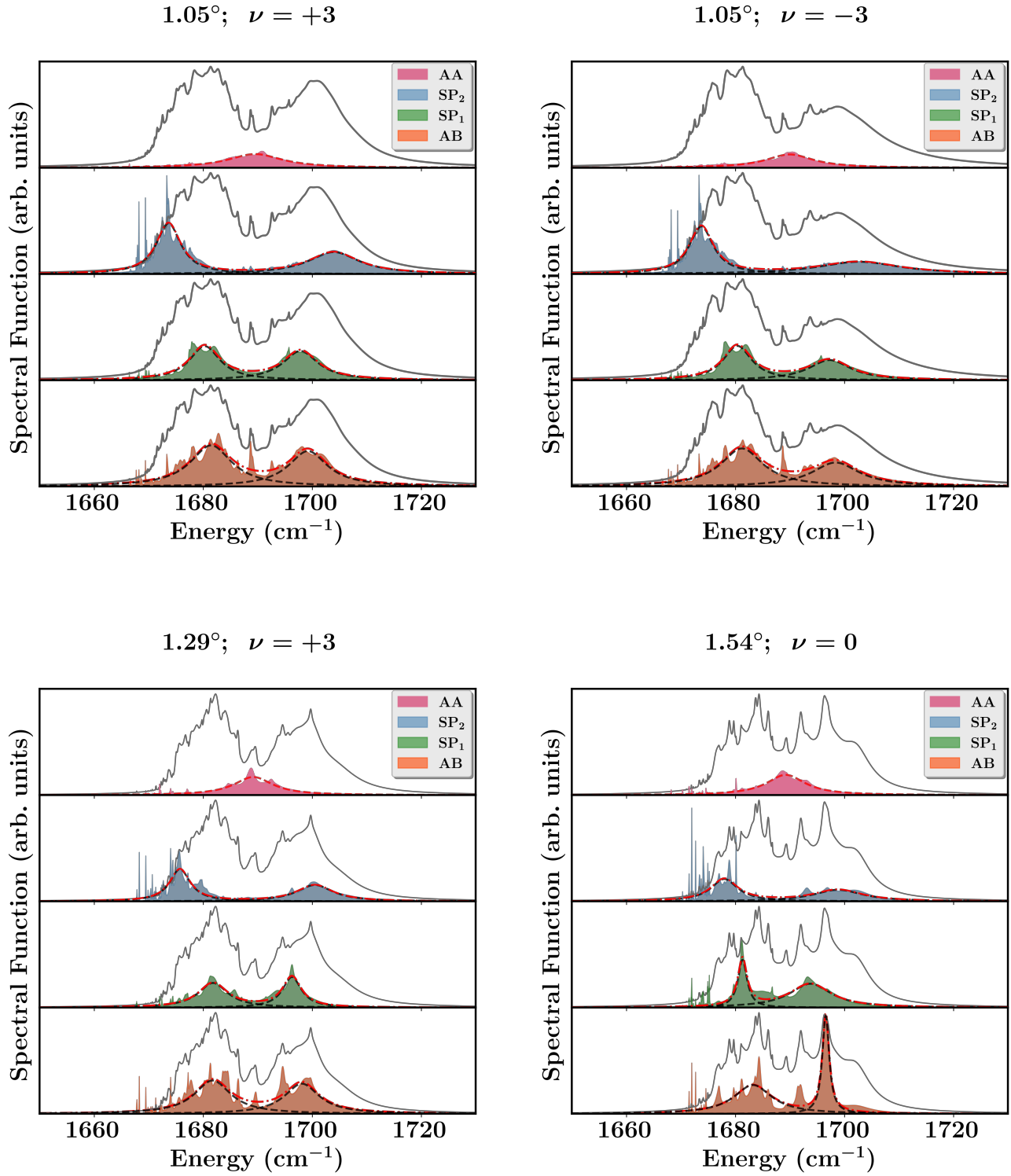


FIG. S8. The projections onto different stacking regions are shown for some angles at different dopings. The total spectrum is marked in each of the panels

JOINT DENSITY OF STATES

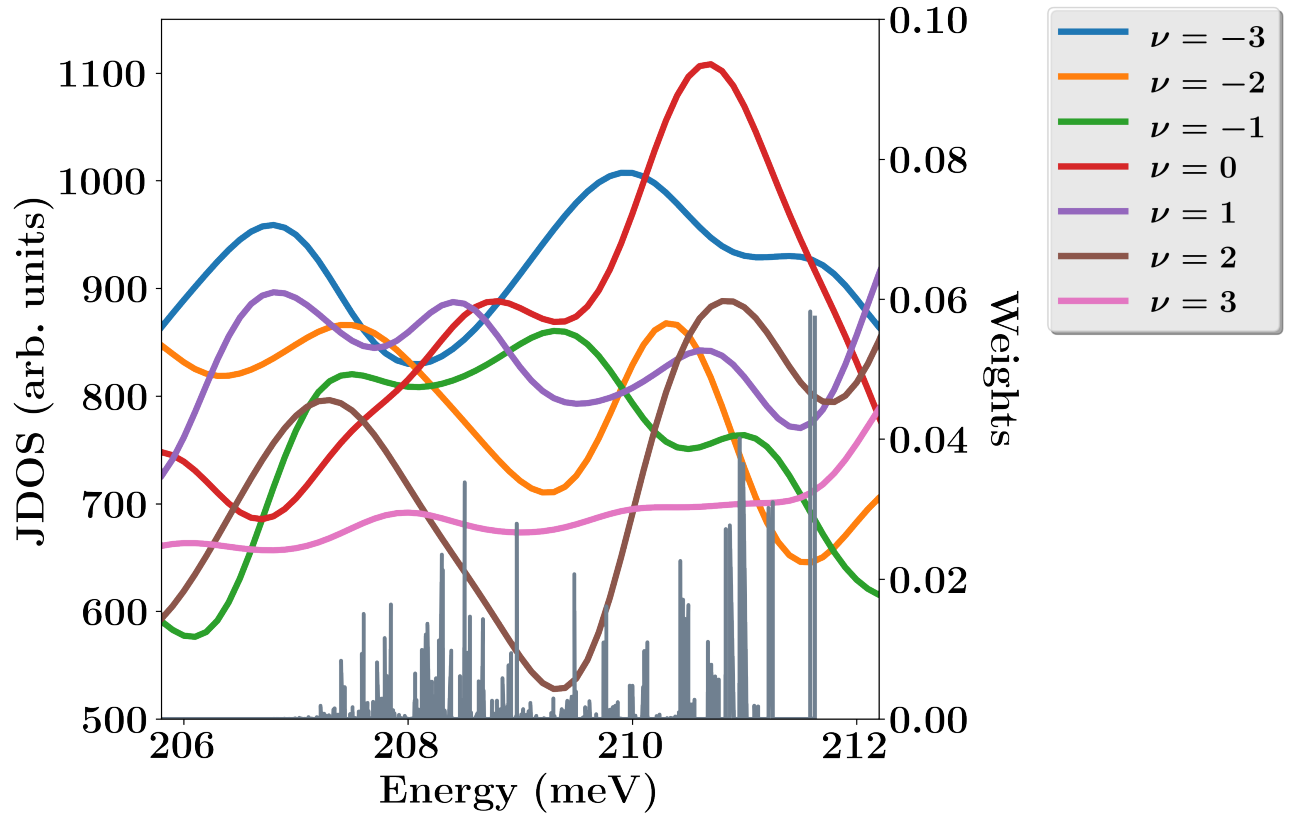


FIG. S9. Joint Density of States $[J(\omega) = \sum_{m,n,\mathbf{k}} (f_{\mathbf{k}}^n - f_{\mathbf{k}}^m) \delta(\epsilon_{\mathbf{k}}^m - \epsilon_{\mathbf{k}}^n - \omega)]$ for 1.05° TBG at different integer fillings. The projected weights of each of the moiré phonon modes onto the bilayer like E_g^+ mode is shown by the grey lines. The apparent anomaly in the abrupt increase in the linewidth of the E_g^+ mode (fig. 2a in the main manuscript) can be explained by looking at the position of the E_g^+ weights and the peaks in the joint density of states. The peak in the moiré mode projections corresponding to the E_g^+ mode aligns with the peak in the joint density of states at $\nu = 0$ (the red curve). This causes an enhancement of the E_g^+ linewidth for 1.05° TBG at charge neutrality.

CONTRIBUTION OF THE HARTREE INTERACTIONS TO THE EL-PH COUPLING

Within a localized orbital framework, the electron-phonon coupling matrix elements arise from all the changes in the Hamiltonian due to the atomic displacements corresponding to the phonon modes [11]

$$g_{\mathbf{k},\mathbf{q}}^{mns} = l_{\mathbf{q}s} \sum_{\kappa\alpha} \Psi_{\mathbf{q}s,\kappa\alpha}^M \sum_{pp';ij} e^{i\mathbf{k}\mathbf{R}_p} e^{-i(\mathbf{k}+\mathbf{q})\mathbf{R}_{p'}} \phi_{\mathbf{k}+\mathbf{q},mj}^* \phi_{\mathbf{k},ni} \langle \Phi_j; \mathbf{R}_{p'} | \frac{\partial \hat{\mathbf{H}}}{\partial \tau_0^{\kappa,\alpha}} | \Phi_i; \mathbf{R}_p \rangle \quad (8)$$

where $|\Phi_i; \mathbf{R}_p\rangle$ denotes the orbital at τ_{pi} and $\tau_{pi} = \tau_{0i} + \mathbf{R}_p$. The coefficients of the electron orbitals in this basis are denoted by $\phi_{\mathbf{k},ni} = e^{-i\mathbf{k}\mathbf{R}_p} \langle \Phi_i; \mathbf{R}_p | n\mathbf{k} \rangle$.

Substituting the non-interacting tight binding model without any interactions,

$$\hat{\mathbf{H}} = \sum_{p\kappa;p'\kappa'} t(\tau_p^\kappa - \tau_{p'}^{\kappa'}) | \Phi_\kappa; \mathbf{R}_p \rangle \langle \Phi_{\kappa'}; \mathbf{R}_{p'} | \quad (9)$$

we get the contribution from the transfer integral to the electron-phonon coupling matrix element following Refs. [11, 12] and in the notations described in the main text as:

$$g_{\mathbf{k},\mathbf{q}}^{mns}(\text{hop}) = l_{\mathbf{q}s} \sum_{\kappa\alpha} \Psi_{\mathbf{q}s,\kappa\alpha}^M \sum_{pi} \frac{\partial}{\partial x_\alpha} t(\tau_0^\kappa - \tau_p^i) \left(e^{i\mathbf{k}\mathbf{R}_p} \phi_{\mathbf{k}+\mathbf{q},m\kappa}^* \phi_{\mathbf{k},ni} + e^{-i(\mathbf{k}+\mathbf{q})\mathbf{R}_p} \phi_{\mathbf{k}+\mathbf{q},mi}^* \phi_{\mathbf{k},n\kappa} \right) \quad (10)$$

When the Hamiltonian has the additional onsite potential (arising from the electron-electron interactions) at each atomic site,

$$\hat{\mathbf{H}} = \sum_{p\kappa;p'\kappa'} t(\tau_p^\kappa - \tau_{p'}^{\kappa'}) | \Phi_\kappa; \mathbf{R}_p \rangle \langle \Phi_{\kappa'}; \mathbf{R}_{p'} | + \sum_{p\kappa} \epsilon_\kappa | \Phi_\kappa; \mathbf{R}_p \rangle \langle \Phi_\kappa; \mathbf{R}_p | \quad (11)$$

there is an additional contribution to the electron-phonon coupling arising from the onsite term:

$$\begin{aligned} g_{\mathbf{k},\mathbf{q}}^{mns}(\text{ons}) &= l_{\mathbf{q}s} \sum_{\kappa\alpha} \Psi_{\mathbf{q}s,\kappa\alpha}^M \sum_{pp';ij} e^{-i(\mathbf{k}+\mathbf{q})\mathbf{R}_p} e^{i\mathbf{k}\mathbf{R}_{p'}} \phi_{\mathbf{k}+\mathbf{q},mj}^* \phi_{\mathbf{k},ni} \sum_{\zeta,\beta} \langle \Phi_j; \mathbf{R}_{p'} | \Phi_\beta; \mathbf{R}_\zeta \rangle \frac{\partial \epsilon_\beta}{\partial \tau_0^{\kappa,\alpha}} \langle \Phi_\beta; \mathbf{R}_\zeta | \Phi_i; \mathbf{R}_p \rangle \\ &= l_{\mathbf{q}s} \sum_{\kappa\alpha} \Psi_{\mathbf{q}s,\kappa\alpha}^M \sum_{pp';ij} e^{-i(\mathbf{k}+\mathbf{q})\mathbf{R}_p} e^{i\mathbf{k}\mathbf{R}_{p'}} \phi_{\mathbf{k}+\mathbf{q},mj}^* \phi_{\mathbf{k},ni} \sum_{\zeta,\beta} \delta_{j,\beta} \delta_{p',\zeta} \frac{\partial \epsilon_\beta}{\partial \tau_0^{\kappa,\alpha}} \delta_{i,\beta} \delta_{p,\zeta} \\ &= l_{\mathbf{q}s} \sum_{\kappa\alpha} \Psi_{\mathbf{q}s,\kappa\alpha}^M \sum_{pp';ij} e^{-i(\mathbf{k}+\mathbf{q})\mathbf{R}_p} e^{i\mathbf{k}\mathbf{R}_{p'}} \phi_{\mathbf{k}+\mathbf{q},mj}^* \phi_{\mathbf{k},ni} \frac{\partial \epsilon_j}{\partial \tau_0^{\kappa,\alpha}} \delta_{i,j} \delta_{p,p'} \\ &= l_{\mathbf{q}s} \sum_{\kappa\alpha} \Psi_{\mathbf{q}s,\kappa\alpha}^M \sum_{p,i} e^{-i\mathbf{q}\mathbf{R}_p} \phi_{\mathbf{k}+\mathbf{q},mi}^* \phi_{\mathbf{k},ni} \frac{\partial \epsilon_i}{\partial \tau_0^{\kappa,\alpha}} \end{aligned} \quad (12)$$

In our work the onsite potential is described by the form proposed by Zachary et. al [9].

$$\begin{aligned} \epsilon_i &= \sum_j (\mathbf{n}_j - \bar{\mathbf{n}}) \sum_{\mathbf{R}_p} W_{\mathbf{R}_p,ij} \\ W_{\mathbf{R}_p,ij} &= \frac{e^2}{4\pi\epsilon_0\epsilon_{\text{bg}}} \sum_{m=-\infty}^{\infty} \frac{(-1)^m}{\sqrt{(\mathbf{R}_p + \tau_0^j - \tau_0^i)^2 + (2m\xi)^2}} \end{aligned} \quad (13)$$

where \mathbf{n}_j is the number density at each atomic site j and $\bar{\mathbf{n}}$ is the average of \mathbf{n}_j . At a filling ν , the average of the number density, $\bar{\mathbf{n}} = 1 + \nu/N$ where N is the total number of atoms in the moiré unit cell. Here we have assumed that the TBG is encapsulated by a dielectric substrate of thickness ξ and dielectric constant ϵ_{bg} . The values of these parameters were obtained from Ref. [9].

The derivative of the onsite potential in eqn.(12) can hence be evaluated as

$$\frac{\partial \epsilon_i}{\partial \tau_0^{\kappa,\alpha}} = \left[\sum_j \frac{\partial (\mathbf{n}_j - \bar{\mathbf{n}})}{\partial \tau_0^{\kappa,\alpha}} \sum_p W_{\mathbf{R}_p,ij} \right] + \left[\sum_j (\mathbf{n}_j - \bar{\mathbf{n}}) \sum_p \frac{\partial W_{\mathbf{R}_p,ij}}{\partial \tau_0^{\kappa,\alpha}} \right] \quad (14)$$

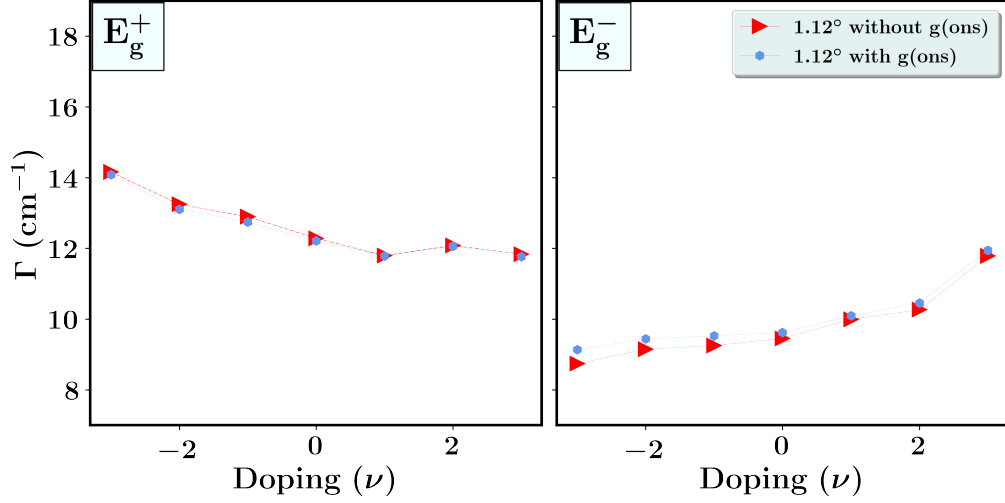


FIG. S10. E_g mode linewidths at 1.12° twist with the correction due to $g_{\mathbf{k},\mathbf{q}}^{mns}(\text{ons})$ included.

The change in the number density $\frac{\partial(\mathbf{n}_j - \bar{\mathbf{n}})}{\partial\tau_0^{\kappa,\alpha}}$ can be safely neglected as this is of higher order in the displacements. Consequently we get

$$\frac{\partial\epsilon_i}{\partial\tau_0^{\kappa,\alpha}} = \sum_j (\mathbf{n}_j - \bar{\mathbf{n}}) \sum_p \frac{\partial W_{\mathbf{R}_p,ij}}{\partial\tau_0^{\kappa,\alpha}} \quad (15)$$

The total electron phonon coupling matrix element is obtained as

$$g_{\mathbf{k},\mathbf{q}}^{mns} = g_{\mathbf{k},\mathbf{q}}^{mns}(\text{hop}) + g_{\mathbf{k},\mathbf{q}}^{mns}(\text{ons}) \quad (16)$$

Within our framework, the addition of the onsite contribution does not result in a significant change to the linewidths obtained, is clear from fig. S10. So it can be concluded that $g_{\mathbf{k},\mathbf{q}}^{mns}(\text{hop})$ is the dominant term.

ANHARMONIC CONTRIBUTION

The anharmonic contribution to the linewidth is computed from the power spectra obtained via the fourier transform of the mode projected velocity autocorrelation function (MVACF) [13]

$$\zeta_{\mathbf{qs}}(\omega) = \int_0^\infty dt \langle \mathbf{V}_{\mathbf{qs}}(0) \mathbf{V}_{\mathbf{qs}}^*(t) \rangle e^{-i\omega t} \quad (17)$$

The MVACF is defined as

$$\langle \mathbf{V}_{\mathbf{qs}}(0) \mathbf{V}_{\mathbf{qs}}^*(t) \rangle = \lim_{\tau \rightarrow \infty} \frac{1}{\tau} \int_0^\tau \mathbf{V}_{\mathbf{qs}}(t') \cdot \mathbf{V}_{\mathbf{qs}}^*(t+t') dt' \quad (18)$$

where the $\mathbf{V}_{\mathbf{qs}}(t)$ is the mode projected velocity defined by

$$\begin{aligned} \mathbf{V}_{\mathbf{qs}}(t) &= \tilde{\mathbf{v}}_{\mathbf{q}}(t) \cdot \hat{\eta}_{\mathbf{qs}} \\ \tilde{\mathbf{v}}_{\mathbf{q}}^\mu(t) &= \sqrt{m_\mu} \sum_j e^{-i\mathbf{q} \cdot \mathbf{r}_j(t)} \mathbf{v}_j(t); \quad j \in \{\text{Atoms of type } \mu\} \end{aligned} \quad (19)$$

where $\mathbf{v}_i(t)$ is the velocity at time t for the particle i , m_μ is the mass of the atom of type μ and $\hat{\eta}_{\mathbf{qs}}$ is the polarization of the unit cell phonon mode (\mathbf{qs}).

In our calculations since we are interested in only the $\mathbf{q} = \mathbf{0}$ phonons, the equations simplify to

$$\begin{aligned} \tilde{\mathbf{v}}_{\mathbf{0}}^\mu(t) &= \sqrt{m_\mu} \sum_j \mathbf{v}_j(t); \quad j \in \{\text{Atoms of type } \mu\} \\ \mathbf{V}_{\mathbf{0s}}(t) &= \tilde{\mathbf{v}}_{\mathbf{0}}(t) \cdot \hat{\eta}_{\mathbf{0s}} \\ \langle \mathbf{V}_{\mathbf{0s}}(0) \mathbf{V}_{\mathbf{0s}}^*(t) \rangle &= \lim_{\tau \rightarrow \infty} \frac{1}{\tau} \int_0^\tau \mathbf{V}_{\mathbf{0s}}(t') \cdot \mathbf{V}_{\mathbf{0s}}^*(t+t') dt' \\ \zeta_{\mathbf{0s}}(\omega) &= \int_0^\infty dt \langle \mathbf{V}_{\mathbf{0s}}(0) \mathbf{V}_{\mathbf{0s}}^*(t) \rangle e^{-i\omega t} \end{aligned} \quad (20)$$

$\Gamma_{\text{ph-ph}}$ is obtained as the FWHM of the Lorentzian fitted to the G mode projected power spectra. The calculations were performed using a system containing 12×12 moiré unit cells for the angles 1.40 and 1.54, and 10×10 moiré unit cells for the other angles. The systems were equilibrated at the final temperature under the NVE ensemble for 100 ps. The velocities of all the atoms were collected every 4 fs for 800 ps in the NPT ensemble.

The fits at the different angles of twist we have considered in our calculations are shown in Fig. S11.

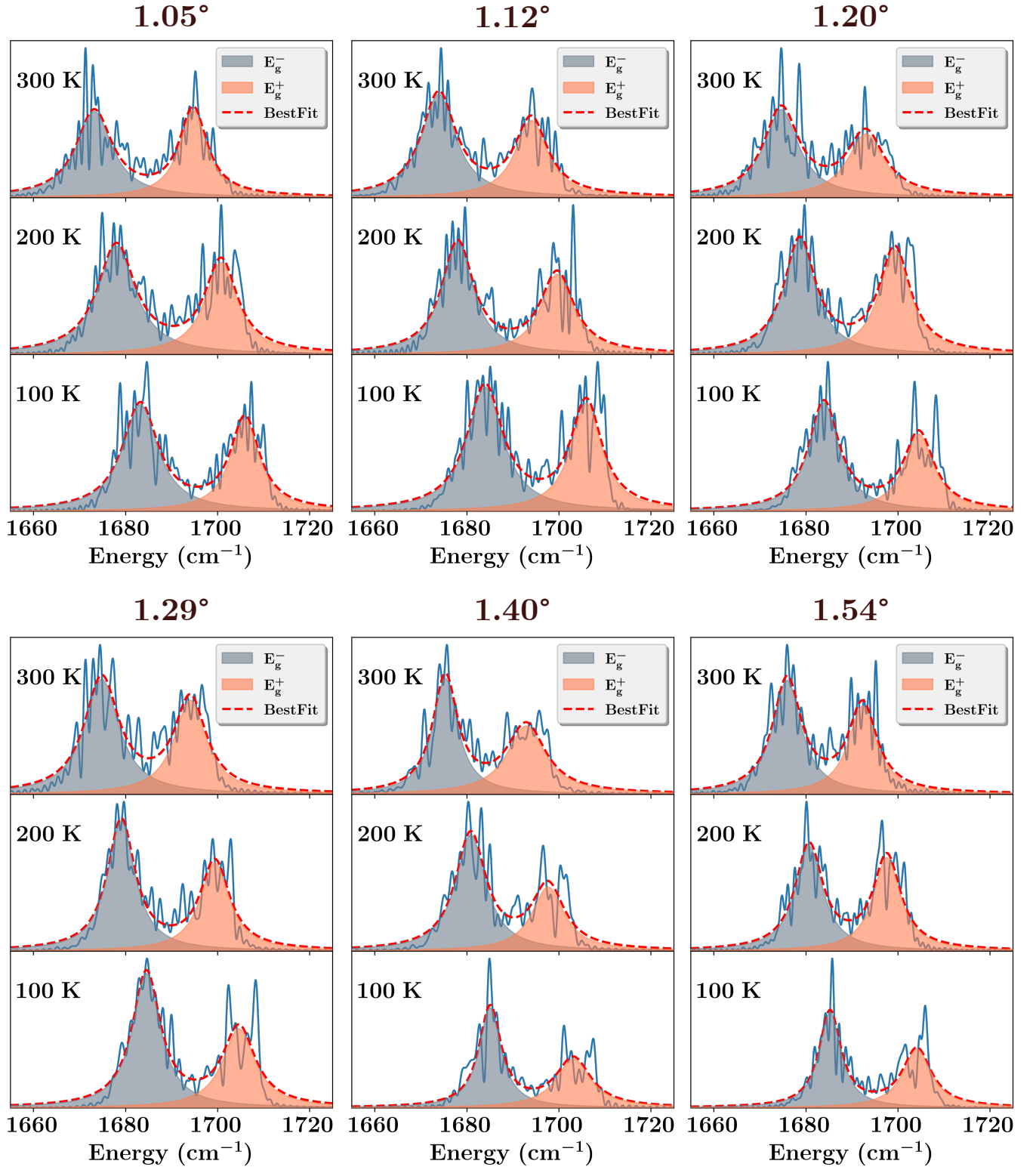


FIG. S11. The fits for the mode projected power spectra at various angles of twist, for different temperatures. The FWHM of these fits give the linewidth while the position of the Lorentzians provide the lineshifts.

* mjain@iisc.ac.in

- [1] S. Naik, M. H. Naik, I. Maity, and M. Jain, *Computer Physics Communications* **271**, 108184 (2022).
- [2] A. P. Thompson, H. M. Aktulga, R. Berger, D. S. Bolintineanu, W. M. Brown, P. S. Crozier, P. J. in't Veld, A. Kohlmeyer, S. G. Moore, T. D. Nguyen, *et al.*, *Computer Physics Communications* **271**, 108171 (2022).
- [3] A. Kmaci, J. B. Haskins, C. Sevik, and T. Çağın, *Physical Review B* **86**, 115410 (2012).
- [4] M. Wen, S. Carr, S. Fang, E. Kaxiras, and E. B. Tadmor, *Physical Review B* **98**, 235404 (2018).
- [5] E. N. Koukaras, G. Kalosakas, C. Galiotis, and K. Papagelis, *Scientific reports* **5**, 12923 (2015).
- [6] J. C. Slater and G. F. Koster, *Physical Review* **94**, 1498 (1954).
- [7] S. Choi, J. Deslippe, R. B. Capaz, and S. G. Louie, *Nano Letters* **13**, 54 (2013).
- [8] P. Moon and M. Koshino, *Physical Review B* **85**, 195458 (2012).
- [9] Z. A. Goodwin, V. Vitale, X. Liang, A. A. Mostofi, and J. Lischner, *Electronic Structure* **2**, 034001 (2020).
- [10] C.-H. Park, F. Giustino, M. L. Cohen, and S. G. Louie, *Nano letters* **8**, 4229 (2008).
- [11] L. A. Agapito and M. Bernardi, *Physical Review B* **97**, 235146 (2018).
- [12] Y. W. Choi and H. J. Choi, *Physical Review B* **98**, 241412 (2018).
- [13] I. Maity, M. H. Naik, P. K. Maiti, H. R. Krishnamurthy, and M. Jain, *Physical Review Research* **2**, 013335 (2020).